Helena Jin · Sanichiro Yoshida
Luciano Lamberti · Ming-Tzer Lin *Editors*

Advancement of Optical Methods in Experimental Mechanics, Volume 3

Proceedings of the 2015 Annual Conference on Experimental and Applied Mechanics

SEM

Springer

Helena Jin • Sanichiro Yoshida • Luciano Lamberti • Ming-Tzer Lin
Editors

Advancement of Optical Methods in Experimental Mechanics, Volume 3

Proceedings of the 2015 Annual Conference on Experimental and Applied Mechanics

Springer

Chapter 35
Strains in Shallow and Deep Notches Using Two DIC Algorithms

G.L.G. Gonzáles, L.D. Rodrigues, M.A. Meggiolaro, and J.L.F. Freire

Abstract In the current work, a high magnification 3D stereoscopic digital image correlation (DIC) system and a 3D micro-stereoscopic DIC system were used to determine elastic and elastic-plastic strain distributions in the proximity of shallow and deep notches. Specimens used were a plate with a shallow circumferential notch under bending load, and two deep U-Notch specimens under tensile load. The data analysis employed two methodologies. One was the direct application of a conventional and commercial DIC analysis tool. Another, applied to the same gathered data, using a novel combination of image analysis technique with a meshless numerical method. The Scale Invariant Feature Transform (SIFT) computer vision algorithm was used to extract distinctive points or features of the captured images. Then, the displacements were obtained by tracking the positions of successfully matched SIFT points of the undeformed-deformed pair of images. In sequence, the points provided by SIFT were selected as nodes of a meshless formulation to generate a numerical approximation of the displacement fields and their derivatives. For that, the moving least square method was employed. The advantages of the novel proposed method were the automaticity in the process correlation and the good performance when low and high strain gradient strain fields co-existed in the same analysis. The SIFT-Meshless strain distributions consistently matched with those obtained from the traditional DIC subset-step type of analysis applied to the same sets of images and with results obtained from finite element models. An important conclusion was that the SIFT-Meshless method provided reliable measurements, especially at the vicinity of the notches where the maximum strain values were expected.

Keywords DIC • SIFT • Meshless • Elasticity • Plasticity • Stress • Concentration • U-notch

35.1 Introduction

Digital Image Correlation (DIC) [1–4] is presently one of the most widely used optical techniques in experimental mechanics. This technique provides full-field displacement and strain measurements of properly prepared prototypes and models by comparing and analyzing two digital images obtained before and after deformation is imposed to the object under observation. The image correlation routine divides the initial image in small regions called subsets, and then every subset is located in the final and correspondent image using a mathematical correlation algorithm.

In DIC applications accurate measurements in high strain gradient fields can be difficult to obtain [5–7], as for example near boundaries in stress concentration problems. The measured gradients near boundary critical points become more flattened than the real ones due to geometric sizes of the used subsets. To minimize these problems, proper subset sizes need to be selected in order to ensure more accurate solutions.

In this work, a combined experimental–numerical technique is presented for strain determination around notches using a novel digital image correlation technique. The proposed technique uses a different approach to the classical subset-based matching for displacement tracking by applying a feature-based matching technique, named Scale-Invariant Feature Transformation. SIFT was proposed by Lowe in 1999 [8–10]. SIFT is a very robust feature-based matching method widely used in several vision-based applications [11, 12], because of its good performance and robustness.

First, the SIFT technique allows the successfully matching of homologous features in the undeformed-deformed pair of images. After, the SIFT matched features are used in a meshless formulation based on the moving least squares (MLS)

G.L.G. Gonzáles • M.A. Meggiolaro • J.L.F. Freire (✉)
Federal University of Pará, UFPA, Rua Augusto Corrêa, 01, Belrém, PA, Brazil
e-mail: giancarlo.g.gonzales@outlook.com; meggi@puc-rio.br; jlfreire@puc-rio.br

L.D. Rodrigues
Federal University of Pará, UFPA, Rua Augusto Corrêa, 01, Belém, PA, Brazil
e-mail: leodr@ufpa.br

method for solving the displacement field and its derivatives. The adopted formulation is similar to the element-free Galerkin (EFG) method proposed by Belytschko [13, 14]. The meshless methods are used here because they do not require a mesh to discretize the problem domain and the approximate solution is constructed entirely using a set of scattered nodes (SIFT points).

The MLS approach consists of a local weighted least square approximation, valid on a small sub domain around the point of interest that only uses the neighborhood information. The flexibility in choosing the size of the sub domains allows performing a self-adapting process in cases where highly nonhomogeneous strain distributions are present.

The aim of this paper is to briefly present the SIFT-Meshless (or simply SIFT-M) digital correlation approach and show its efficiency when applied to in-plane strain measurements on regions of high strain gradients, including under elastoplastic conditions. Three applications using different materials and different types of loading are presented: the elastic problem of deep U-notches in two polycarbonate specimen under uniaxial tensile load; the elastic-plastic problem of a semicircular notch in a steel specimen under bending load; and the elastic-plastic problem of a deep U-notch in an aluminum specimen under uniaxial tensile load. Two other solutions methods were applied to the same problems in order to highlight the efficiency of the proposed SIFT-M method. One was the traditional DIC analysis using the VIC-3D software developed by Correlated solution Inc. [15] which was used employing the same images. The other was the numerical finite element method where the solutions of the elastic and elastic-plastic problems were completed using the ANSYS software.

35.2   Fundamentals of DIC Technique

DIC techniques utilize tracking procedures and image registration techniques to quantify displacement measurements using a single camera for planar measurements (2D) or two cameras for space measurements (3D). The observed surface needs a contrasting speckle pattern applied to it.

DIC compares two or more digital images taken from the material surface at different loading stages. For that, the DIC algorithm divides the reference image (i.e. one image generally acquired in the unloaded stage) in various small regions called subsets. The displacement field is determined through tracking the movement of the speckle pattern using the prescribed subsets observing the reference image and the deformed image. Algorithms such as the normalized cross correlation (NCC), sum of squared differences (SSD), sum of absolute differences (SAD) or variants of these methods can be used to calculate the similarity between the reference subset and the target subset. The corresponding subset location can be determined by searching the maximum or minimum correlation criterion in the specified searching area. From that, the full-field deformation distribution is obtained and the correspondent strain distribution map can then be determined.

For example, Eq. (35.1) shows the NCC function, which is ranked as one of the most effective and commonly used similarity metrics.

$$C\left(x,\ y,\ x',\ y'\right) = \frac{\sum F\left(x, y\right) \cdot G\left(x', y'\right)}{\sqrt{\sum F(x, y)^2 \cdot \sum G\left(x', y'\right)^2}} \tag{35.1}$$

where F(x,y) is the gray value of point (x,y) in the undeformed subset of reference image, and G(x′,y′) is the gray value of point (x′,y′) in the deformed subset of corresponding deformed image.

The distribution of gray level from subset to subset is a discrete function. Continuous gray level distributions can be achieved for both images if the gray level distributions can be smoothed out by some kind of interpolation function. Commonly, a local deformation mapping function is used, which can be solved by using an Iterative Least Squares algorithm.

For example, illustrated in Fig. 35.1, a first order mapping function is written as

$$\begin{aligned} x' &= x + u + u_x \cdot \Delta x + u_y \cdot \Delta y \\ y' &= y + v + v_x \cdot \Delta x + v_y \cdot \Delta y \end{aligned} \tag{35.2}$$

where $\triangle x$, $\triangle y$ are the distances from the subset center to point (x', y'), u and v are the displacement components of the reference subset center in x and y directions, and u_x, u_y, v_x, v_y are the first-order displacement gradients of the reference subset, that make possible the determination of the strain state ε_x, ε_y, ε_{xy}.
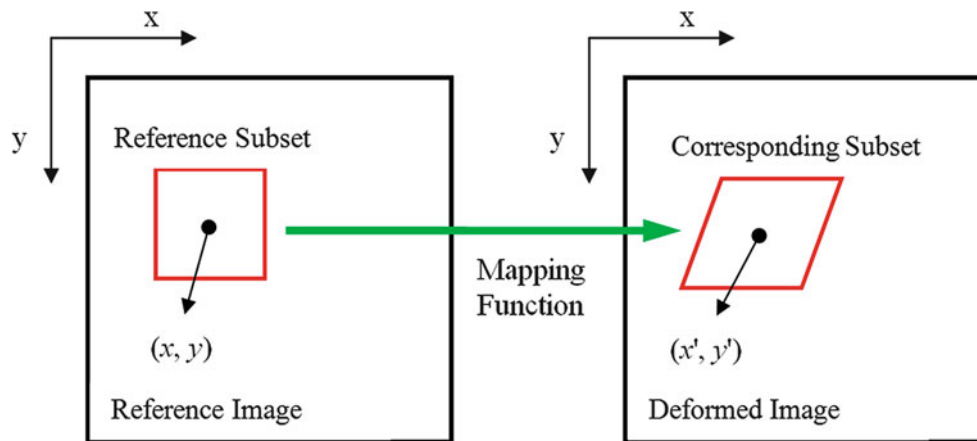
Fig. 35.1 Principle of the digital image correlation technique

35.3 Fundamentals of Proposed SIFT-Meshless Method

The proposed SIFT-Meshless method is divided into two main steps. The experimental displacement measurements using the SIFT technique, and the meshless formulation for modeling the displacement and strain fields.

35.3.1 Displacement Measurements Using SIFT

The SIFT algorithm can detect stable feature points from a single image even though not all of which are useful. Here, the algorithm is used to measure relative displacements of successful feature matches between two images of the specimen surface, one captured before and other after deformation (see Fig. 35.2). In this study, the implementation of the David Lowe's SIFT algorithm is used [16].

The tracking feature procedure based on the SIFT algorithm involves three steps: feature detection, feature description, and feature matching (more detailed information about the SIFT algorithm can be found in [10]), described as follows.

In the feature detection step, points of interest are detected using a robust cascade filtering. A detailed model is fit to determine position, scale, and contrast, during which some candidate points are discarded based on measures of their stability.

In the feature description step, a local descriptor for each feature point is computed. The descriptor is a vector of 128 elements that describes a small region around the feature point using a 3D histogram of gradients, locations, and orientations.

In the feature matching step, the best match for each descriptor is found using the nearest neighbor distance (closest descriptor) in the database of feature descriptors from the processed images. In order to discard poorly or too ambiguous matched features, a subsequent threshold is used. If the distance ratio between the closest neighbor and the second-closest neighbor is below some threshold, then the match is kept; otherwise, the match is rejected and the feature is removed. In common SIFT applications, a distance ratio between 0.6 and 0.8 is used, as recommended by Lowe. In the present experimentation, due to the large number of points extracted from images, a distance ratio of 0.3–0.4 is found to lead to good results.

Moreover, since a stereovision system is used to capture the images, a stereo calibration process has to be performed before the experiment. For the correspondence problem, the SIFT technique is also used to determine matches in the left and right camera images. Finally, the information of calibration and correspondence step are used to recover the 3D position from the 2D image point pair based on a stereo triangulation algorithm.

35.3.2 Meshless Formulation

Once the SIFT features are located in the undeformed-deformed pair of images, they are selected as field nodes in a meshless formulation. Thus, the u-component of the displacement field at an arbitrary point $\mathbf{x}^{\mathrm{T}} = [x, y, z]$ in the problem domain is

Fig. 35.2 Displacement
measurements by matching SIFT
features

Reference Image   Deformed Image
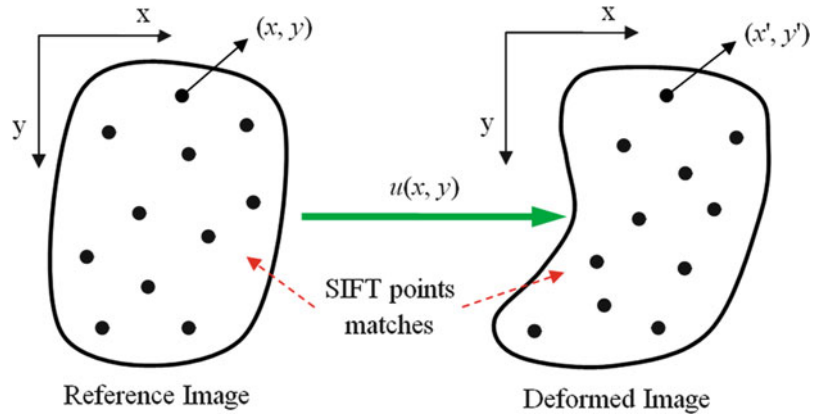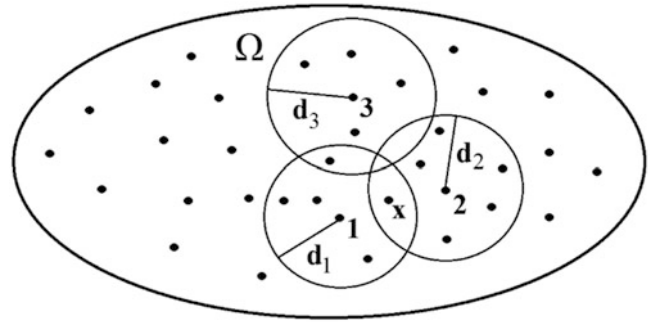
Fig. 35.3 Circular influence
domains for the nodes 1, 2 and 3
with radius of domain d_1, d_2 and
d_3, respectively

approximated with $u^h(\mathbf{x})$ using the nodal displacements within a local domain or small neighborhood around the point $\mathbf{x}$.
Mathematically,

$$u^h(\mathbf{x}) = \sum_i^n \phi_i(\mathbf{x}) \, u_i \tag{35.3}$$

where n is the number of nodes in the local domain of $\mathbf{x}$, $\phi_i(\mathbf{x})$ is the shape function of the ith node, and u_i represents the
nodal displacements provided by tracking SIFT features.

35.3.2.1 Influence Domain

The shape functions are said to be locally supported, because only a determined set of field nodes around point $\mathbf{x}$ are used to
support or approximate the function value at $\mathbf{x}$. For domains with irregularly distributed nodes (such as the SIFT features),
the use of an influence domain works well to select nodes for approximations. The influence domain represents the region
where a node exerts its influence, and it is defined for each node in the problem domain. Circular or rectangular domain
shapes are the mostly often used. In this work, a circular shape was adopted, as shown in Fig. 35.3.

In Fig. 35.3, the node termed $\mathbf{x}$ is within the influence domain of the nodes 1 and 2. Later these nodes will be used to
construct the shape function of the point $\mathbf{x}$. The node 3 will be not used because it does not have any influence on point $\mathbf{x}$.

The dimension of the influence domain determines the number of nodes to be used to approximate the value of the field
function at any given point $\mathbf{x}$. These approximants are constructed by using a weight function with compact support. Several
weight functions are presented in the literature, e.g., [17]. Here, the exponential weight function Eq. (35.4) was adopted.

$$w(r) = \begin{cases} e^{-(r/0.4)^2}, & r \leq 1 \\ 0, & r > 1 \end{cases} \tag{35.4}$$

The dimension of r is calculated by the equation:

$$r = \frac{\|\mathbf{x} - \mathbf{x}_i\|}{dm_i} \tag{35.5}$$

For a point of interest at $\mathbf{x}$, the dimension of the influence domain, dm_i, is determined by

$$dm_i = \alpha_s \cdot d_i \tag{35.6}$$

where d_i is the radius of domain that defines the minimum number of nodes used for approximation, and α_s is a scaling parameter.

According to literature [18] and experimental results conducted by the authors, values $\alpha_s = 2.0$ through 4.0 are suggested. If the influence domain is too small ($\alpha_s < 2.0$), there are not enough nodes to perform the function approximation for the field variables. On the other hand, if the influence domain is too large ($\alpha_s > 4.0$), the constructed shape functions becomes too smooth to characterize the local properties of the field variables.

35.3.2.2   MLS Approximation

The meshless shape functions are constructed based on the moving least squares MLS strategy and obtained by

$$u^h(\mathbf{x}) = \sum_{j}^{m} p_j(\mathbf{x}) \; a_j(\mathbf{x}) = \mathbf{P}^{\mathrm{T}}(\mathbf{x}) \; \mathbf{a}(\mathbf{x}) \tag{35.7}$$

where $\mathbf{P}^{\mathrm{T}}(\mathbf{x})$ is a polynomial basis of order m (e.g. linear, quadratic)

$$\mathbf{P}^{\mathrm{T}}(\mathbf{x}) = \begin{bmatrix} p_1(x) \; p_2(x) \; \dots \; p_m(x) \end{bmatrix} \tag{35.8}$$

and $\mathbf{a}(\mathbf{x})$ is a vector of coefficients to be determined.

$$\mathbf{a}(\mathbf{x}) = \begin{bmatrix} a_1(x) \; a_2(x) \; \dots \; a_m(x) \end{bmatrix}^{\mathrm{T}} \tag{35.9}$$

The unknown coefficients $\mathbf{a}(\mathbf{x})$ are obtained by minimizing the difference between the local approximation and the function, denoted by J, through

$$J = \sum_{i}^{n} w(\mathbf{x} - \mathbf{x}_i) \begin{bmatrix} \mathbf{P}^{\mathrm{T}}(\mathbf{x}_i) \; \mathbf{a}(\mathbf{x}) - u_i \end{bmatrix}^2 \tag{35.10}$$

where $w(\mathbf{x} - \mathbf{x}_i)$ is the weight function and n is the number of points in the neighborhood of $\mathbf{x}$ for which the weight function $w(\mathbf{x} - \mathbf{x}_i) \neq 0$.

Minimizing J in order to determine the unknown parameters, $\mathbf{a}(\mathbf{x})$, results in the following linear system:

$$\mathbf{a}(\mathbf{x}) = \mathbf{A}^{-1}(\mathbf{x}) \; \mathbf{B}(\mathbf{x}) \; \mathbf{U} \tag{35.11}$$

where the matrices A and B are defined by

$$\mathbf{A}(\mathbf{x}) = \sum_{i=1}^{n} w(\mathbf{x} - \mathbf{x}_i) \; \mathbf{P}(\mathbf{x}_i) \; \mathbf{P}^{\mathrm{T}}(\mathbf{x}_i) \tag{35.12}$$

$$\mathbf{B}(\mathbf{x}) = \begin{bmatrix} w(\mathbf{x} - \mathbf{x}_1) \; \mathbf{P}^{\mathrm{T}}(\mathbf{x}_1) \; w(\mathbf{x} - \mathbf{x}_2) \; \mathbf{P}^{\mathrm{T}}(\mathbf{x}_2) \; \dots \; w(\mathbf{x} - \mathbf{x}_n) \; \mathbf{P}^{\mathrm{T}}(\mathbf{x}_n) \end{bmatrix} \tag{35.13}$$

and the vector $\mathbf{U}$ contains all the nodal displacements:

$$\mathbf{U} = \sum_{i}^{n} u_i \tag{35.14}$$

Note that the matrix **A** will be regular, i.e. invertible. From Eq. (35.12), it can be seen that the minimum number of nodes depends on the polynomial basis function used. In this work, a quadratic basis two-dimensional function was used.

$$\mathbf{P}^{\mathrm{T}}(\mathbf{x}) = \begin{bmatrix} 1 & x & y & xy & x^2 & y^2 \end{bmatrix} \tag{35.15}$$

After, substituting Eq. (35.11) into Eq. (35.7), the MLS approximation is obtained

$$u^h(\mathbf{x}) = \sum_i^n \sum_j^m p_j(\mathbf{x}) \left[\mathbf{A}^{-1}(\mathbf{x})\mathbf{B}(\mathbf{x})\right]_{ji} u_i \tag{35.16}$$

where, by comparing with Eq. (35.3), the shape function ϕ_i associated with the node $\mathbf{x}_i$ is defined by

$$\phi_i(\mathbf{x}) = \sum_j^m p_j(\mathbf{x}) \left(\mathbf{A}^{-1}(\mathbf{x})\mathbf{B}(\mathbf{x})\right)_{ji} \tag{35.17}$$

This can be written shortly as

$$\phi_i = \mathbf{P}^{\mathrm{T}} \mathbf{A}^{-1} \mathbf{B}_i \tag{35.18}$$

Eq. (35.3) can also be used for the displacement component $v(\mathbf{x})$, i.e.

$$v(\mathbf{x}) = \sum_i^n \phi_i(\mathbf{x}) \, v_i \tag{35.19}$$

Thus, the displacement field in the deformed surface is approximated and defined as

$$\begin{Bmatrix} u \\ v \end{Bmatrix}^h = \sum_i^n \begin{bmatrix} \phi_i & 0 \\ 0 & \phi_i \end{bmatrix} \begin{Bmatrix} u_i \\ v_i \end{Bmatrix} \tag{35.20}$$

The (small) strains at any point in the problem domain are obtained in terms of the nodal displacement components by:

$$\begin{Bmatrix} \varepsilon_x \\ \varepsilon_y \\ \varepsilon_{xy} \end{Bmatrix}^h = \begin{bmatrix} \frac{\delta}{\delta x} & 0 \\ 0 & \frac{\delta}{\delta y} \\ \frac{\delta}{\delta y} & \frac{\delta}{\delta x} \end{bmatrix} \begin{Bmatrix} u \\ v \end{Bmatrix}^h \tag{35.21}$$

Combining Eq. (35.21) in Eq. (35.20), the first order partial derivatives of the MLS shape with respect to x and a y direction are required,

$$\begin{Bmatrix} \varepsilon_x \\ \varepsilon_y \\ \varepsilon_{xy} \end{Bmatrix}^h = \sum_i^n \begin{bmatrix} \phi_{i,x} & 0 \\ 0 & \phi_{i,y} \\ \phi_{i,y} & \phi_{i,x} \end{bmatrix} \begin{Bmatrix} u_i \\ v_i \end{Bmatrix} \tag{35.22}$$

where, the spatial derivatives are obtained by

$$\phi_{i,\,x} = \mathbf{P}^{\mathrm{T}}_{,x}\mathbf{A}^{-1}\mathbf{B}_i + \mathbf{P}^{\mathrm{T}}\left(\mathbf{A}^{-1}\right)_{,x}\mathbf{B}_i + \mathbf{P}^{\mathrm{T}}\mathbf{A}^{-1}\mathbf{B}_{i,x} \tag{35.23}$$

$$\phi_{i,\,y} = \mathbf{P}^{\mathrm{T}}_{,y}\mathbf{A}^{-1}\mathbf{B}_i + \mathbf{P}^{\mathrm{T}}\left(\mathbf{A}^{-1}\right)_{,y}\mathbf{B}_i + \mathbf{P}^{\mathrm{T}}\mathbf{A}^{-1}\mathbf{B}_{i,y} \tag{35.24}$$

Thereby, Eq. (35.20) and Eq. (35.22) can be implemented to compute the displacement and strain fields, respectively, for a given pair of undeformed-deformed images. It is worth mentioning that the small-strain approximation defined in Eq. (35.22) is used for strains less than 1 %.

Fig. 35.4 Test function for calculate the values of α_s parameter
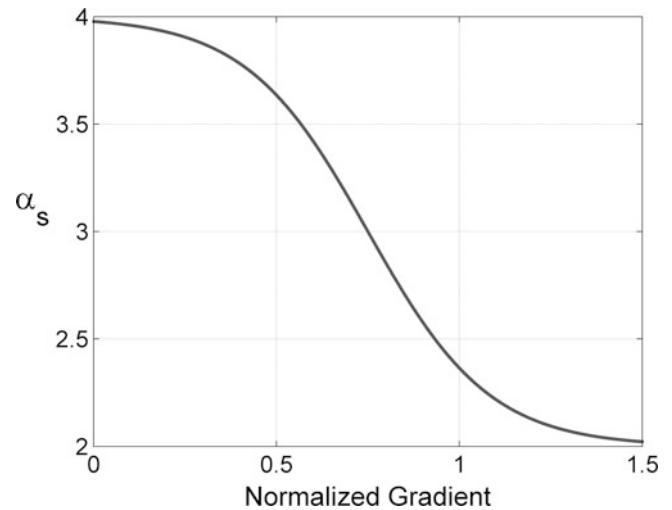
35.3.2.3 Variable Domain of Influence

In the MLS approximation, a suitable influence domain is required to make a stable and accurate solution. Referring to Eq. (35.6), it can be seen that the parameter α_s is a multiplier support that controls the actual dimension of the domain. The dimensionless size of α_s should be pre-determined by the analyst. Generally, values of $\alpha_s = 2.0$ through 4.0 are used for static analysis.

In this study, because of the high density of SIFT points extracted from images, the minimum number of nodes is set to be much larger than the minimum requirements (with neighborhoods not less than 100 nodes). Therefore, the size of influence domain is established to be variable. The aim of this variability is to get more accurate results by decreasing the supporting nodes for approximation in areas with high stress concentration, in which higher accuracy is required. On the other hand, the number of nodes increases in areas where the stress distribution is uniform, and thus a smoothed solution is provided.

For this purpose, a methodology was established to automatically determine the α_s values for each supported node. First, a meshless approximation is computed with a high value of α_s, such as 4.0. Then, the gradient of this first approximation is computed in the direction of the notch. The magnitude of the gradient will show how fast the strain rises in that direction, indicating areas of high strain concentration.

This information is useful for choosing a suitable value of α_s at each evaluation point, using for that a test function similar to one shown in Fig. 35.4. This function was tested and behaved satisfactorily in numerical simulations using bench-mark problems for which solutions were known beforehand. Lastly, the approximations are re-computed with the new values of α_s, and the corresponding strain distribution on the surface is obtained.

35.4 Experimental Procedure

35.4.1 Data Acquisition

The 3D image acquisition process uses two synchronized cameras coupled with high magnification lenses observing the material surface during the experiment from different directions. Two data acquisition systems were used: a high magnification stereoscopic system for the measurement of areas with side-lengths ranging from 5 to 50 mm, and a micro-stereoscopic system for the measurement of areas with side-lengths ranging from 1 to 7 mm. The used digital CCD (charge-coupled device) cameras have resolutions of 2448×2048 pixels. The VIC-Snap was the software used to acquire the image pairs and to synchronize them with the computer. The sample surface was illuminated using a fiber-optic light source to improve the quality of acquired images.

The calibration of the stereovision systems was completed in the calibration module of VIC-3D software. In this procedure, calibration plates from Correlated Solutions were used. They were positioned in front of the cameras at the
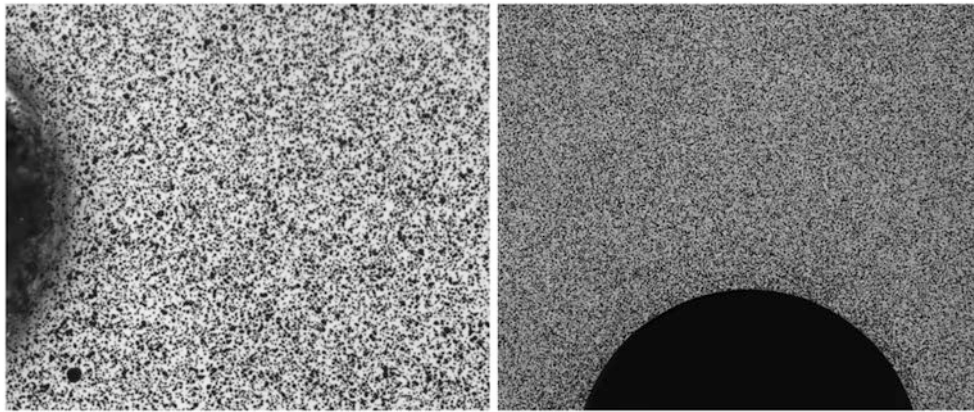
Fig. 35.5 Specimen preparation at micro- and macro-scales

same position of the specimen to be tested. Each calibration plate contains a grid of dots target with known sizes and locations. The parameters of the camera systems are recovered from the detection and recognition of these targets using stereo mathematical models. Thereafter, this information is useful to recover the 3D positions of the images captured by the cameras using a stereo triangulation algorithm. The quality of the camera calibration is an important factor that determines the accuracy of the vision system.

35.4.2 Specimen Preparation

The sample surface was previously prepared for the proper functioning of both techniques. In the traditional digital image correlation approach, this procedure aims to create a random pattern with high contrast on the specimen surface. In the SIFT-Meshless method, the surface preparation aims to provide a large number of possible points of interest that can be detected by the SIFT algorithm.

According to that, the samples surfaces were covered firstly with a uniform white paint and thereafter, black dots are inserted. The size and distribution of dots influences the achievable resolution. At macroscopic length scales, the random black-and-white pattern was performed with a colored spray paint. At microscopic length scales, small dots were obtained with an airbrush system that provides a smooth transition from fine to medium spraying. The surface specimen preparations used for the two stereoscopic systems used are shown in Fig. 35.5.

35.5 Strain Concentration Under Elastic Conditions in a Tensile Test

35.5.1 Experimental Conditions

The test performed in this section aimed to determine elastic strain distribution in a small region of high strain gradient, i.e., close to the notch root. For that, two specimens of polycarbonate with thickness of 3 mm and containing central deep U-notches with radii of 2.4 mm (PC-1) and 1 mm (PC-2) were tested under tension. The geometry of the two polycarbonate specimens is shown in Fig. 35.6, where the y-axis is the loading axis.

The experimental setup used a load frame, a load cell and the micro-stereoscopic system. Successive loads of 25, 50, 100 N were applied to PC-1, and 15, 30, 60 N to PC-2. The loads were applied to the specimens through pins inserted into holes at midpoints close to the specimens' extremities. For each increment of force, its corresponding image was captured. The high magnification micro-stereoscopic system permitted deformation measurement within a pixel resolution of 2.5 μm.

Fig. 35.6 Sketch of the experimental set-up of PC-1 specimen (r = 2.4 mm, h = 24.7 mm) and of PC-2 specimen (r = 1 mm, h = 30.2 mm)
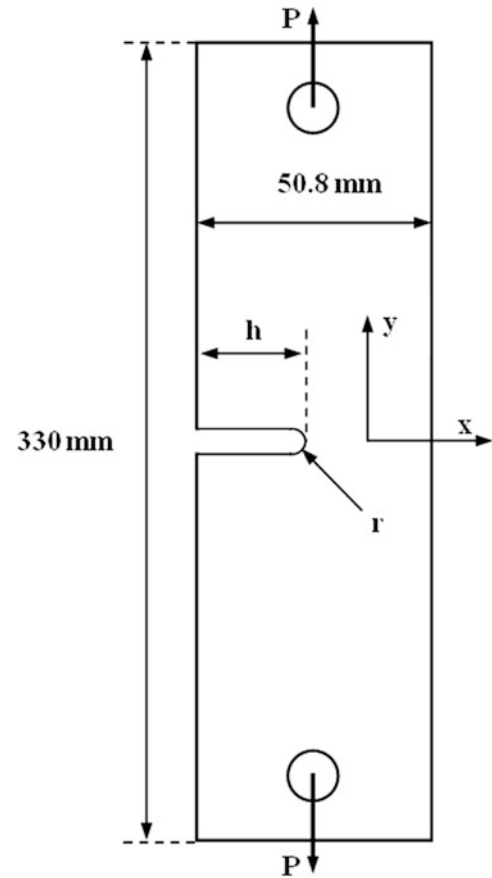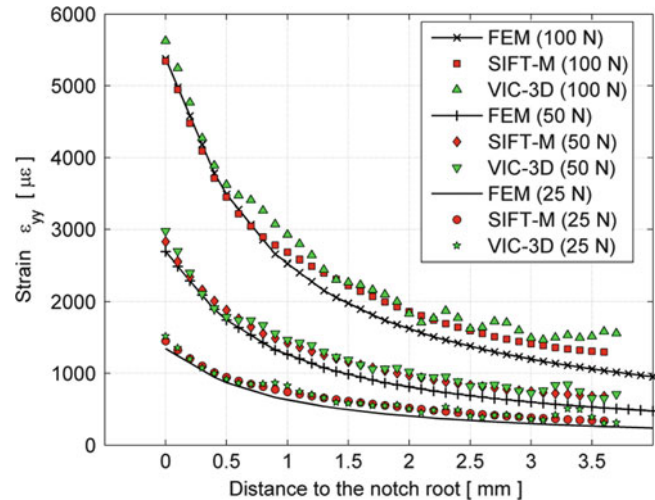

Fig. 35.7 Specimen PC-1: stress distribution along distance from the notch root determined by numerical and the experimental methods


35.5.2 Results

Surface strains around the notch were assessed with the VIC-3D software using subset sizes of 43×43 and 49×49 pixels for PC-1 and PC-2, respectively. The step size was set to 8 pixels for both analyses. In SIFT-Meshless analysis, the minimum domain was set to 0.5 mm.

Figures 35.7 and 35.8 show the longitudinal strain values determined by the VIC-3D and SIFT-Meshless approaches along the x-axis of the net section of the specimens at position $y = 0$. The maximum strains occur at the notch root for each load applied. In addition, the strain distributions were compared with results determined by the finite element simulation. The experimental and numerical results show good agreement between them.

Fig. 35.8 Specimen PC-2: stress
distribution along distance from
the notch root determined by
numerical and the experimental
methods
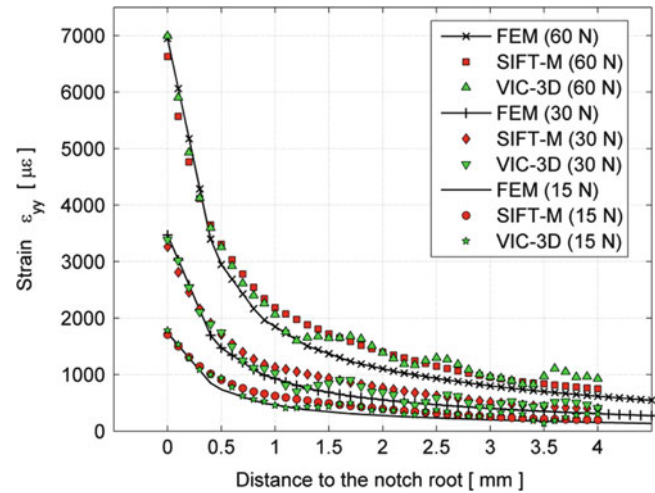
From the test results, it can be seen that the strain concentration is more severe in PC-2 on which, for the maximum loading of 60 N, the measured strain value varies drastically from 0.2 to 0.7 % inside a distance of approximately 1 mm from the notch root. Moreover, a proportional ratio is found between the maximum strain values at notch root and the applied load, due to the linear elastic behavior of the polycarbonate specimen during the tensile test.

35.6 Strain Concentration Under Elastic-Plastic Conditions in a Bending Test

35.6.1 Experimental Conditions

A four-point bending test was conducted in a 304 stainless-steel plate with a semicircular notch located in the center of the specimen bottom edge. The steel sample had thickness of 5 mm and notch radius of 12.5 mm. The specimen dimensions and the four-point bending setup are shown schematically in Fig. 35.9. The Modulus of Elasticity (E) was determinate to be 195 MPa and the yield stress $S_{y,\,0.2\%}$ was found to be 250 MPa. These material properties were determined by an uniaxial tension test.

The bending test was performed in a servo-hydraulic Instron machine equipped with a four-point bending fixture. The inner and outer spans were fixed at 80 and 160 mm, respectively as shown in Fig. 35.9. The cameras were placed in front of the specimen in a stereo configuration by using a tripod. The optical configuration resulted in a field of view of about 35×30 mm with a pixel resolution of 14 μm on the object plane. Images were taken from the specimen with loadings of 4, 6, 8 and 10 kN, whereby the elastic limit was attained and plastic strains at notch root were expected.

35.6.2 Results

After capture, the images were processed using VIC-3D software with a subset size of 25×25 pixels, and a step size of 11 pixels was used. The minimum domain used in the SIFT-Meshless method was set to 2.5 mm. The Finite Element simulation was carried out simulating the same loading 4-point bending setup. The numerical solution used an isotropic multilinear model, described by the plastic stress-strain curve of the material obtained from the tensile test. The maximum strain values plotted in Fig. 35.10 indicate that significant plastic strain at the notch root occurred after the load of 6 kN was reached.

Figure 35.11 shows the axial strain values determined by the VIC-3D and SIFT-Meshless methods along the *y*-axis of the net section at position $x = 0$ for each load applied. In the same figure are included the numerical results obtained using the finite element software ANSYS.

Fig. 35.9 Sketch of the experimental setup of the 4-point bending specimen PC-3
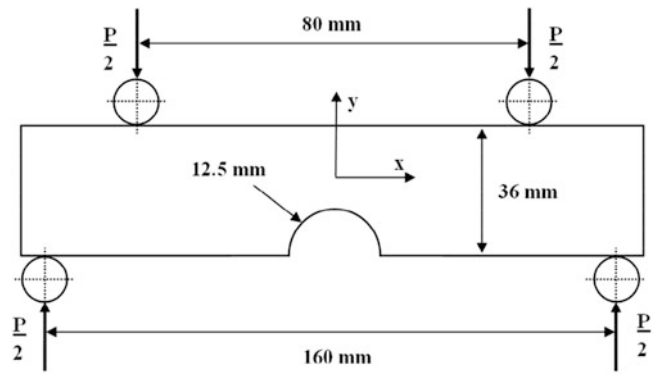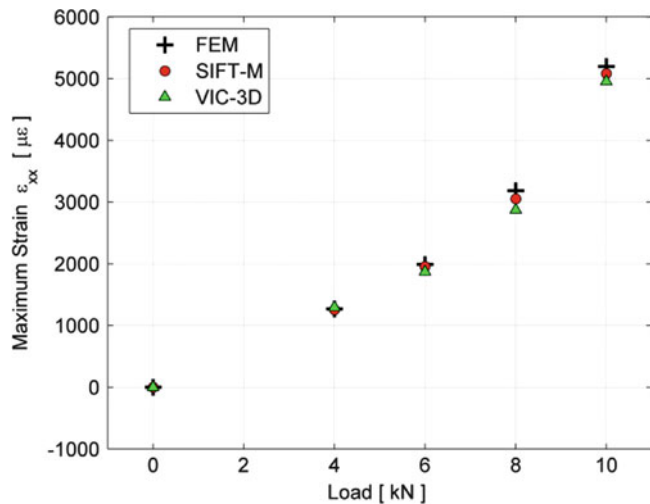

Fig. 35.10 Maximum strain evolution for ε_{xx}

The distributions plotted in Fig. 35.11 show that the experimental and numerical results presented the same trend. The two experimental techniques were able to follow the evolution of plastic strains at the notch root during loading, where the magnitude of plastic strain reached approximately 0.3 % when the test load was 10 kN.

Figure 35.11 shows that the VIC-3D response presented a waviness shape. The nearest point to the notch edge was located at about 250 μm from it and this distance was caused by the subset size chosen for the DIC analysis. The results determined using the SIFT-Meshless method were close to and in good agreement with the simulation results obtained using the ANSYS software including points close to the notch zone.

35.7   Strain Concentration Under Elastic-Plastic Conditions in a Tensile Test

35.7.1   *Experimental Conditions*

In order to quantify plastic strain around a high strain gradient region, a tensile test was performed on an aluminum plate with a central deep U-notch of radius 1 mm. The specimen geometry and dimensions are shown schematically in Fig. 35.12. The yield stress of the aluminum sample $S_{y, 0.2\%}$ was found from a uniaxial tension tests and it was equal to 127 MPa.

In this test, the specimen was first loaded to 1200 N and then unloaded. After, the reference image was captured in the unloaded stage and then a new loading event of 0–1400 N–0 by 200 N steps was applied. At each load increment or decrement, the corresponding deformed image was captured.
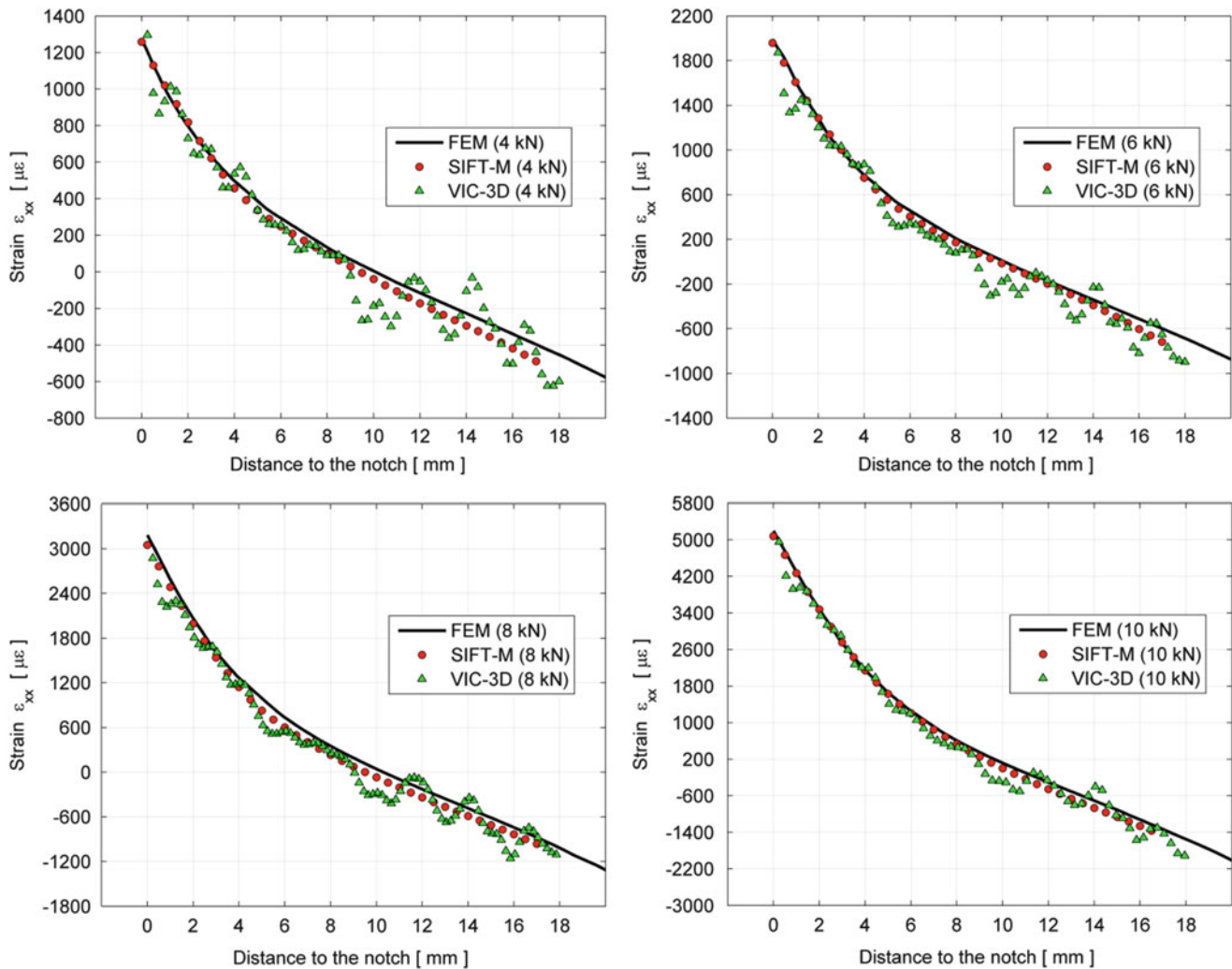
Fig. 35.11 Axial strain distribution along the *x*-axis

35.7.2　Results

Recorded images from the tests were processed using the VIC-3D software with subset size and step respectively equal to 45×45 pixels and of 11 pixels. The same gathered images were processed using the SIFT-Meshless method using a minimum domain of 0.5 mm.

The variation of the maximum strain measured at notch root with applied load is plotted in Fig. 35.13. The experimental values show an elastic behavior up to the load value of 1200 N, reached in the previously event. Above 1200 N and up to the maximum load of 1400 N is visible in the complete loading and unloading cycle shown in Fig. 35.13.

The strain distribution values measured by the VIC-3D and SIFT-Meshless methods along the *x*-axis of the net section at position $y = 0$ for the maximum loading of 1400 N are shown in Fig. 35.14. A good agreement is found between the responses measured by two experimental techniques. One can see that there is a large change in strain within 1 mm from the notch root, where the measured strain values vary from 0.3 to 0.8 %.

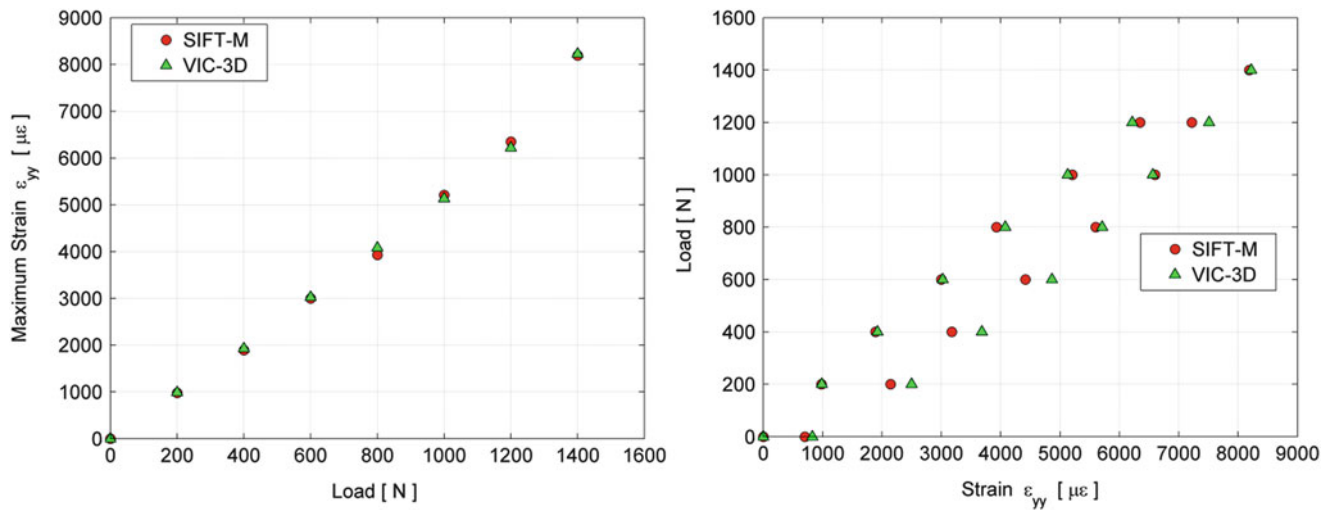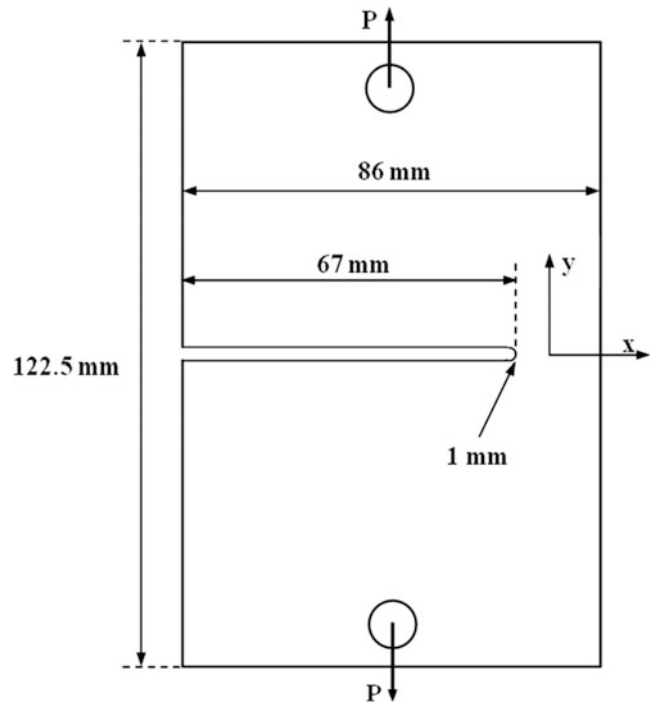**Fig. 35.12** Sketch of the experimental setup for PC-4

Fig. 35.13 Maximum strain variation at with applied load at the for ε_{xx}

35.8   Conclusion

In the present work, the SIFT-Meshless method was introduced and successfully tested to correlate and analyze images. It was applied to determine displacement and strain fields in elastic and elastic-plastic problems in high strain gradient regions near to discontinuities. Three notched specimens of different materials: polycarbonate, stainless steel, and aluminum were tested under different types of loading. It was shown that the use of the SIFT technique allows for displacement measurements in the notch edge boundaries, since features were detected in these regions. Moreover, the proposed meshless formulation employed a variable and sizable influence domain that adapted the calculation of solutions to the presence of low and high strain gradients in the same specimen. Elastic and plastic measured strain values as high as 0.8 % confirmed the validity of the method. The SIFT-Meshless results agreed satisfactorily with results achieved with applications of the traditional DIC method that used previously defined subset and step sizes, as well as with numerical finite element analysis results that were obtained by applying a commercial software.

Fig. 35.14 Axial strain
distribution along the *x*-axis
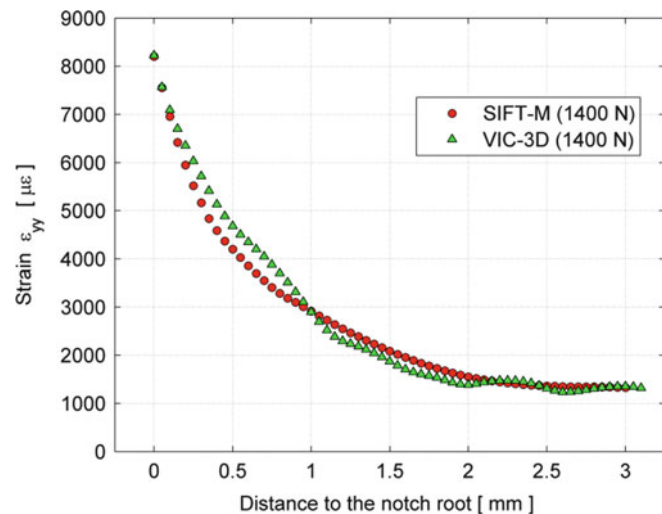
References

1. Peters, W.H., Ranson, W.F., Sutton, M.A., Chu, T.C., Anderson, J.: Application of digital correlation methods to rigid body mechanics. Opt. Eng. **22**(6), 738–742 (1983)
2. Peters, W.H., Ranson, W.F.: Digital imaging techniques in experimental stress analysis. Opt. Eng. **21**(3), 427–431 (1982)
3. Sutton, M.A., Wolters, W.J., Peters, W.H., Ranson, W.F., McNeill, S.R.: Determination of displacements using an improved digital correlation method. Image Vis. Comput. **1**(3), 133–139 (1983)
4. Sutton, M.A., Orteu, J.J., Schreier, H.: Image Correlation for Shape, Motion and Deformation Measurements: Basic Concepts, Theory and Applications. Springer, New York, NY (2009)
5. Hwang, S.-F., Wu, W.-J.: Deformation measurement around a high strain-gradient region using a digital image correlation method. J. Mech. Sci. Technol. **26**(10), 3169–3175 (2012)
6. Lagattu, F., Brillaud, J., Lafarie-Frenot, M.-C.: High strain gradient measurements by using digital image correlation technique. Mater. Charact. **53**(1), 17–28 (2004)
7. Qian, C., Harper, L.T., Turner, T.A., Warrior, N.A.: Notched behaviour of discontinuous carbon fibre composites: comparison with quasi-isotropic non-crimp fabric. Compos. A: Appl. Sci. Manuf. **42**(3), 293–302 (2011)
8. D.G. Lowe, *Object recognition from local scale-invariant features. Proceeding of the International Conference on Computer Vision*, 1999, pp. 1150–1157
9. D.G Lowe, *Local feature view clustering for 3D object recognition. Proceedings of the 2001 IEEE Computer Society Conference*, 2001
10. Lowe, D.G.: Distinctive image features from scale-invariant keypoints. Int. J. Comput. Vis. **60**(2), 91–110 (2004)
11. Castle, R.O., Murray, D.W.: Keyframe-based recognition and localization during video-rate parallel tracking and mapping. Image Vis. Comput. **29**(8), 524–532 (2011)
12. Lee, Y.-J., Song, J.-B.: Autonomous salient feature detection through salient cues in an HSV color space for visual indoor simultaneous localization and mapping. Adv. Robot. **24**(11), 1595–1613 (2010)
13. Belytschko, T., Lu, Y.Y., Gu, L.: Element-free Galerkin methods. Int. J. Numer. Methods Eng. **37**(2), 229–256 (1994)
14. Dolbow, J., Belytschko, T.: An introduction to programming the meshless Element Free Galerkin method. Arch. Comput. Meth. Eng. **5**(3), 207–241 (1998)
15. Solutions, C.: VIC-3D Manual. Correlated Solutions. Inc., Columbia, SC (2010)
16. D., Lowe, *Demo software: sift keypoint detector, 2008*. (2011). Demo available for download at http://www.cs.ubc.ca/~lowe/keypoints
17. Belytschko, T., Organ, D., Krongauz, Y.: A coupled finite element-element-free Galerkin method. Comput. Mech. **17**(3), 186–195 (1995)
18. Liu, G.-R.: Meshfree Methods: Moving Beyond the Finite Element Method. CRC press, Boca Raton, FL (2010)